Eychenne, J., Rust, A., Cashman, K., & Wobrock, W. (2017). Distal Enhanced Sedimentation From Volcanic Plumes: Insights From the Secondary Mass Maxima in the 1992 Mount Spurr Fallout Deposits. *Journal of Geophysical Research: Solid Earth*, *122*(10), 7679-7697. https://doi.org/10.1002/2017JB014412

Distal enhanced sedimentation from volcanic plumes: insights from the secondary mass maxima in the 1992 Mount Spurr fallout deposits

Julia Eychenne [ab*], Alison Rust [b], Katharine Cashman [b], Wolfram Wobrock[c]

[a] Laboratoire Magmas et Volcans, Université Clermont Auvergne - CNRS - IRD, OPGC, Campus Universitaire des Cézeaux, 6 Avenue Blaise Pascal, 63178 Aubière Cedex

[b] School of Earth Sciences, University of Bristol, United Kingdom

[c] Laboratoire de Météorologie Physique, Université Clermont Auvergne - CNRS, OPGC, Campus Universitaire des Cézeaux, 4 Avenue Blaise Pascal, 63178 Aubière Cedex

* Corresponding author: julia.eychenne@uca.fr

Key points

Areas of Secondary Mass Maximum (ASMM) in tephra fallout deposits do not always result from preferential settling of ash <125 µm in size relative to coarser grain sizes

Bimodal Total Grain Size Distributions of eruptions can affect the sedimentological pattern of the tephra fallout deposits

Topography-induced perturbations of the wind field generate turbulence above rough terrain which can accelerate the transfer of particles towards the low atmospheric layers

Abstract

Some tephra fallout deposits show an increase of mass and thickness at distances from the source > 100 km (Areas of Secondary Mass Maximum, ASMM) which demonstrates distal enhanced sedimentation from volcanic plumes. We explore development of the ASMMs during the 1992 August and September Mount Spurr eruptions, U.S.A by combining field data on the spatial distribution of mass and grain size with (1) simulations of individual particle settling through a homogeneous and horizontally stratified atmosphere and (2) mesoscale models of the three-dimensional wind field that include the effect of the underlying topography. The crosswind and downwind variations of deposit characteristics indicate that the increase of sedimentation at the ASMMs are not formed solely because of preferential settling of small ash particles (<125 μm), as commonly assumed in aggregation models. Instead, ASMM grain sizes correspond to the fine modes of the bimodal Total Grain Size Distributions (TGSDs). There also appears to be a link between the ASMM and the topography: the mass local minima occur across the windward flank of 2 km-high mountain ranges, while the ASMMs spread on the leeward flank. Mesoscale models of the three-dimensional wind field show vertical oscillations in the wind over mountainous regions, which may enhance mechanisms of en-masse sedimentation (aggregation, hydrometer formation, particle boundary layers) as well as strong spatial variations of the horizontal wind field in the lower troposphere. Our study demonstrates the importance of using grain size, as well as mass, data to constrain the complex processes responsible for particle sedimentation from volcanic plumes.

1- Introduction

Explosive volcanic eruptions inject large amounts of fragmented material (tephra) into Earth's atmosphere, which are subsequently dispersed by the winds. Dispersion and sedimentation of tephra plumes through the atmosphere can disturb aviation airspace (Kueppers et al. 2014; Webley 2015), destroy crops and infrastructure on the ground and cause adverse respiratory effects (e.g., Horwell and Baxter 2006; Jenkins et al. 2015; Wilson et al. 2015). A critical aspect of volcanology is thus to understand the physical processes controlling the atmospheric path of tephra, which depends strongly on the plume depletion during dispersion, i.e. the fallout of tephra to the ground (e.g., Bursik et al. 1992; Sparks et al. 1992). New field and experimental evidence demonstrates that the sedimentation mechanisms controlling plume depletion can be complex. In particular, the fall of individual particles through the atmosphere at their terminal velocity only partially describes the settling behaviour of tephra (e.g., Del Bello et al. 2017), while additional collective sedimentation processes such as aggregation (e.g., Taddeucci et al. 2011; Bagheri et al. 2016) and en-masse collapse of gravitational instabilities (e.g., Durant et al. 2009; Carazzo and Jellinek 2012; 2013; Manzella et al. 2015) can be significant.

Sedimentation of tephra on the ground forms cone- to sheet-like fallout deposits that thin exponentially over several hundreds of kilometres (e.g., Pyle 1989; Walker 1981). However, several sheet-like tephra fallout deposits show a local increase of mass and thickness at distal locations (Brazier et al. 1983; Brown et al. 2012; Carey and Sigurdsson 1982; Hildreth and Drake 1992; Sarna-Wojcicki et al. 1981), hereafter referred to as Areas of Secondary Mass Maximum (ASMM). There are clear ASMMs in fallout deposits from the 1932 eruption of Quizapu, Chile (Hildreth and Drake 1992; Larsson 1937), the May 18, 1980 Mount St. Helens eruption, U.S.A. (Sarna-Wojcicki et al. 1981), the June 3, 1991 Unzen eruption, Japan

(Watanabe et al. 1999), the August and September, 1992 Spurr eruptions, U.S.A. (McGimsey et al. 2001), and a ~9.75 ka Chaitén eruption, Chile (Watt et al. 2015). There are also complex distal depositional patterns sometimes considered to be ASMMs, such as in the 1991 Hudson, Chile (Scasso et al. 1994), 1991 Pinatubo, Philippines (Wiesner et al. 2004) and 2008 Chaiten, Chile fallout deposits (Watt et al. 2009). The presence of ASMMs in fallout deposits indicates that enhanced deposition of tephra can occur locally after the plume has spread to great distances (> 100 km). This demonstrates unambiguously that sedimentation of tephra is not solely controlled by the fall of individual particles through a constant atmosphere. Understanding the mechanisms producing ASMMs can thus bring valuable insights into particle sedimentation processes, and improve physical models of volcanic plume dispersion and depletion.

Here we explore a range of processes that can affect the dispersion and sedimentation of volcanic plumes and assess their importance in the formation of ASMMs. We focus on the 1992 August and September eruptions of Mount Spurr, Alaska, which produced exceptionally well documented fallout deposits and conspicuous ASMMs at distances greater than 150 km from vent (McGimsey et al. 2001). Processes of ash deposition for both eruptions have previously been modelled by Durant and Rose (2009) assuming single spherical particles falling through an atmosphere considered as a stack of homogeneous horizontal layers. They showed that this simple approach overestimates the settling distance of fine ash compared to the observed grain size in the deposits. They explain the discrepancy using thermodynamic modelling of the September plume, which indicates that ice-coated ash hydrometeors could have formed near the tropopause, allowing for later sublimation and en-masse sedimentation from the plume base (Durant and Rose 2009). The September Spurr ASMM has also been reproduced numerically using the tephra transport and sedimentation models FALL3D and Ash3d (Folch et al. 2010;

Mastin et al. 2016), both of which include ash aggregation. Confirmation of complex ash deposition during the Spurr eruptions comes from shape analyses and terminal fall velocity measurements in the laboratory on a tephra sample from the distal end of the ASMM of the August deposit, which show that particles with a wide range of shape, density and terminal velocity settled at a single location (Riley et al. 2003).

Here we extend these studies using crosswind and downwind variations of both mass and grain size within the deposits. Like Durant and Rose (2009), we use both numerical simulations of individual particle settling through a simplified and horizontally stratified atmosphere; our approach differs in exploring the effects of particle shape on settling velocity. We also model the three-dimensional wind field at the mesoscale to assess the impact of the underlying topography on atmospheric turbulence and particle transport. We then use these results to assess the effects of different scenarios of distal enhanced sedimentation on the characteristics (location and grain size) of the ASMMs. We conclude that, in contrast to existing models of particle aggregation, all grain sizes present in the plume at the relevant distance from vent are contributing to the mass increase on the ground, and that both the Total Grain Size Distribution (TGSD) generated at the vent and topography-induced perturbations of the wind field may play important, and often ignored, roles in controlling depositional patterns of tephra.

2- Models of aggregation, ASMM formation and impact on deposit trends

Aggregation models for ASMM formation

The first conceptual and semi-empirical model of ASMM formation was developed to explain the trends in the fallout deposit from the 18 May, 1980, Mount St. Helens (MSH) eruption, where a clear ASMM is located ~300 km from the vent (Sarna-Wojcicki et al. 1981). Bimodal grain size distributions were also observed in the ASMM, which suggested that the two features

were related (Carey and Sigurdsson 1982; Brazier et al. 1983). Early numerical simulations of the dispersion and sedimentation of the MSH plume reproduced the lateral mass variation of the deposit along the axis by assuming that all fine ash (i.e. particles < 63 μm in size) aggregated in clusters falling individually at a velocity of 0.35 m/s (Carey and Sigurdsson 1982). Based on this study, and the real time observations of 250 to 500 μm clumps falling from the MSH plume ~400 km from vent (Sorem 1982), Brazier et al. (1983) suggested that the fine grain size mode was generated by ash settling as aggregates that formed the ASMM. Brazier et al. (1983) extended this analysis to other fall deposits and concluded that grain size bimodality in individual samples from fall deposits is due to a single process – aggregation - and suggested that ASMMs would be observed in more fallout deposits if they were documented more distally.

The idea that aggregation causes ASMMs is now widespread (e.g., Brown et al. 2012). We illustrate this conceptual model by examining the expected variations of both Mass per unit Area (MpuA) and the proportion of fine ash (<63 μm, i.e. >4 Φ as $\Phi = -log_2$*(particle diameter in mm)*) along the fallout deposit axis (Fig. 1). In the ideal context of (1) a unimodal source grain size distribution and (2) individual particle sedimentation from a volcanic plume spreading in a constant wind field, an exponentially thinning deposit is produced (Fig. 1A). The proportion of fine ash increases linearly with distance and reaches 100 % after the plume is entirely depleted in particles coarser than 63 μm. Under the same conditions, aggregation will create an ASMM only if the aggregates generated in the dispersing plume are restricted to a narrow range of size and density that causes them to fall in a limited area rather than spreading through the deposit (Fig. 1B).

The inferred link between aggregation and ASMM formation has led to a practice of using mass distributions (MpuA) within deposits to calibrate models of ash aggregation (e.g., Carey and

142 Sigurdsson 1982; Cornell et al. 1983; Costa et al. 2010; Folch et al. 2010; Mastin et al. 2016).
143 The September deposit of the Spurr eruption has been a particular focus of such studies in recent
144 years. For example, Mastin et al. (2016) use the Spurr deposit to calibrate an empirical ash
145 aggregation scheme, which attributes all fine ash and 50% of the 3Φ (125 μm) size class to
146 aggregates with a narrow Gaussian size distribution (tests standard deviation of 0, 0.1, 0.2 and
147 0.3 Φ and means from 1.9 to 3.1Φ) and density of 600 kg/m^3. The best fit to the Spurr deposit,
148 which corresponds to an aggregate size distribution with mean = 2.4Φ and standard deviation
149 = 0.1Φ, substantially underestimates MpuA along the dispersal axis; the same approach to the
150 1980 MSH deposit strongly underestimates the distal ash load. A sophisticated wet aggregation
151 scheme was introduced by Costa et al. (2010) and applied to the September Spurr deposit by
152 Folch et al. (2010). The best fit of the simulations to MpuA data from the Spurr deposit is for
153 aggregates with component grains with a fractal dimension of 3 (which is the maximum
154 possible value, corresponding to a size distribution that can completely fill a space) and falling
155 velocity of 0.29 times that of a non-porous sphere of the same diameter as the aggregate. This
156 scheme predicts that only 23, 22, 32, 54 and 45% of the particles 125, 63, 32, 15.6 and 8 μm in
157 size will form aggregates in the 2Φ class (250-500 μm) for this eruption, and so some very fine
158 ash falls as individual particles. The inclusion of this aggregation scheme in the model generates
159 a prominent ASMM and substantially improves agreement with the overall set of deposit MpuA
160 data points, although the misfit for some individual locations is worse with aggregation.
161
162 Observational evidence shows that, both in the field (Sorem 1982; Bonadonna et al. 2002;
163 Taddeucci et al. 2011; Bagheri et al. 2016) and in the laboratory (Gilbert and Lane 1994; James
164 et al. 2002; 2003; Van Eaton et al. 2012), wet and dry clustering mechanisms actually generate
165 a wide range of aggregate types, shapes, sizes and densities. Although there is no reason to
166 expect that all aggregate types will be produced during a single eruption (e.g., Brown et al.

2012), generation of only a single class of aggregates (in terms of size, density and shape) is also highly unlikely (e.g., Bonadonna et al. 2002). In fact, models that assume aggregates of a single (Folch et al., 2010) or very limited (Mastin et al., 2016) range in size and/or density should produce an abrupt and distal increase of MpuA that correlates directly with an increase in the proportion of fine ash (Fig. 1B). Moreover, where not all particles in a given size class are included in the aggregates, sedimentation should resume as settling of individual particles, and the transition from aggregate to individual particle should produce an abrupt decrease of MpuA, closing the ASMM (Fig. 1B). From a grain size perspective, particles that are included in aggregates should show some premature deposition relative to their calculated settling velocities, and these particle sizes should be in the deposit beyond the ASMM in accordance with single-particle settling (but in diminished quantity compared to without aggregation). In particular, the proportion of fine ash should decrease abruptly beyond the ASMM limit of aggregation-assisted settling before increasing with distance (Fig. 1B). Consequently, in ASMMs produced only by model aggregation processes, the proportion of fine ash should follow the mass variations within the ASMM. Assessing the accuracy of such models thus requires comparison not only of modelled and observed MpuA, but also of grain size data at individual locations in the deposit. Importantly, a recent study shows that incorporation of grain size data into an inversion scheme also improves mass estimates, even when aggregation is not important (White et al. 2017).

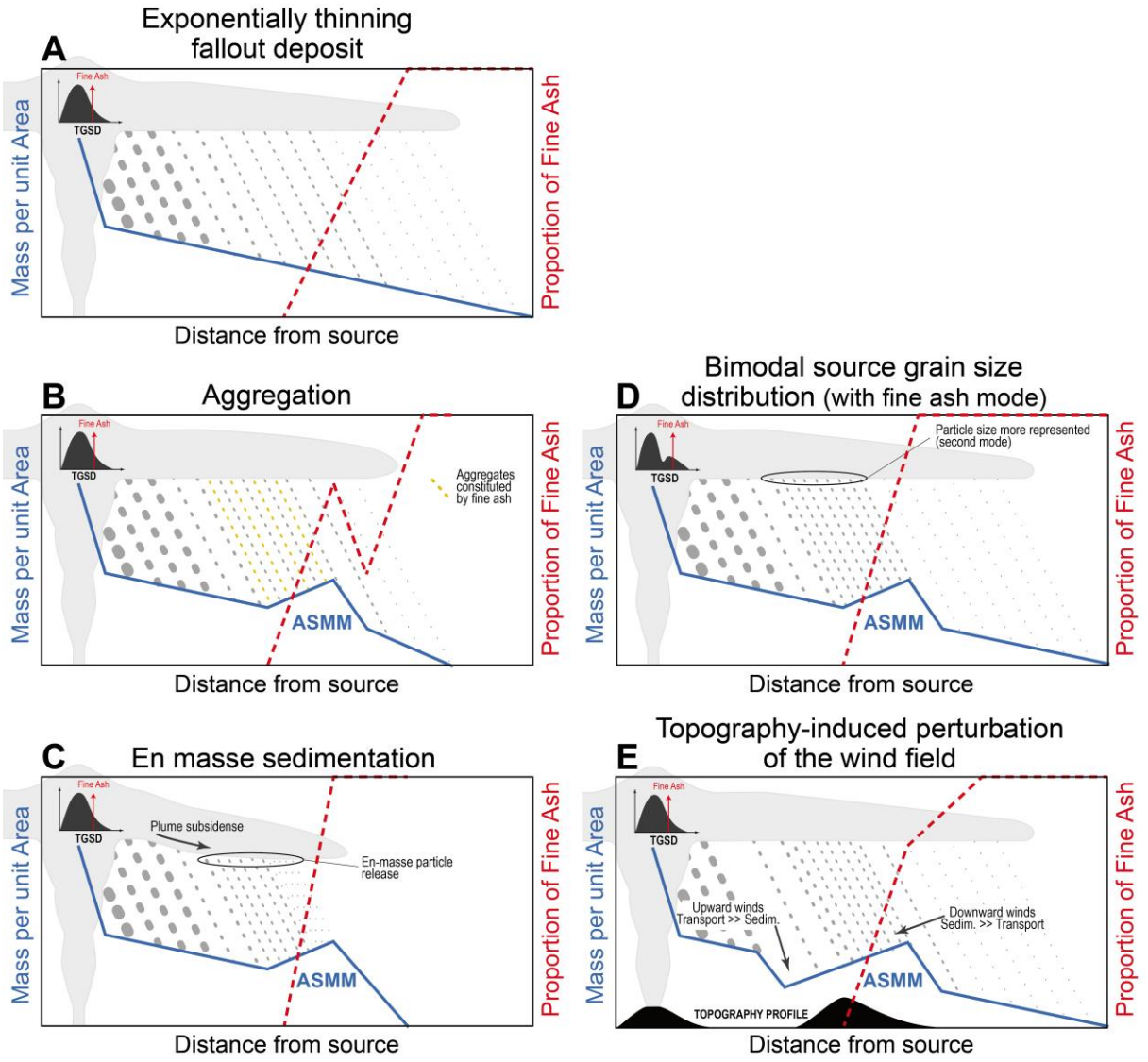

187

188 ***Figure 1:*** *Schematic of the variations of mass and fine ash content (i.e. particles < 63 µm in*
189 *size) in fallout deposits expected for different atmospheric and source conditions, and different*
190 *sedimentation behaviours. The blue and red dotted lines represent the variations of MpuA (left*
191 *axis) and proportion of fine ash (right axis), respectively. The cartoons in the background*
192 *represent schematically the settling of particles from a spreading volcanic plume.*

193

194 *Additional contributions to ASMM formation*

195 As illustrated above, ASMMs provide insights not only into the distal dispersion and
196 sedimentation behaviour of volcanic plumes, but can also improve our understanding of ash

aggregation. Here we turn the question around, to examine mechanisms of ASMM formation that may be independent of aggregation. Interestingly, numerical simulations of the September 1992 Spurr eruption produce an ASMM at about the right distance from source without including aggregation, although in this case the modelled ASMM is deficient in mass relative to the observations (Folch et al. 2010). Here the ASMM forms as a consequence of the Total Grain Size Distribution (TGSD) of the eruption, which is bimodal because of enrichment in fine ash (Rose and Durant 2009). Interestingly, other deposits with bimodal TGSDs also show ASMMs, including that of 1980 MSH, where bimodality, aggregation and ASMMs were originally linked (Carey and Sigurdsson, 1982; Brazier et al., 1983). In this case, the grain size bimodality of the deposit results from mixing of ash contributions from two different sources (fine-grained co-blast and coarser vent-derived plumes; Eychenne et al. 2015). These examples highlight mechanisms other than aggregation alone that can both enhance distal tephra sedimentation and produce ASMMs.

To illustrate the effects of different enhanced sedimentation mechanisms on ASMM formation and deposit-wide patterns of grain size variations, we consider how the ideal depositional pattern in Fig. 1A would be affected by (1) variations in initial conditions and (2) different dispersion and sedimentation scenarios. The case of a bimodal TGSD is shown in Figure 1D. Here, simplistically, each grain size mode is assumed to produce a mass mode at the depositional distance corresponding to the settling of individual grains of that size; the maximum size mode will therefore create the ASMM. In this example, the proportion of fine ash should increase smoothly with distance at a rate that depends on the rate of grain size change for $\Phi>4$. En-masse sedimentation is another suggested mechanism of premature fine ash deposition (Carazzo and Jellinek, 2013; Manzella et al., 2015) and ASMM formation (Durant et al., 2008; Durant and Rose, 2009). The latter has been attributed to microphysical processes of ice coating ash in a moist atmosphere followed by sublimation or melting of the

hydrometeors, which can trigger rapid en-masse sedimentation of the gravitationally unstable lower portion of the cloud (Durant and Rose 2009; Durant et al. 2009). En-masse sedimentation should cause a rapid release of all particle sizes locally present in the plume to form an ASMM with a wide size range and a rapid increase in the proportion of fine ash coincident with the ASMM (Fig. 1C). A final mechanism for ASMM formation is topography-induced perturbation of the wind field that increases upward wind velocities on windward sides of mountains, and downward wind velocities on lee sides (Jiang and Doyle 2004; Watt et al. 2015). Such perturbations of wind velocities can retain tephra in suspension on the windward sides of mountains while enhancing tephra sedimentation on the lee sides (Watt et al. 2015; Poulidis et al. 2017). In this case, we would expect the deposited mass of tephra to decrease rapidly upwind of an ASMM, for the ASMM to be located downwind of a topography high, and for the proportion of fine ash to increase within the ASMM (Fig. 1E).

3- Background on the 1992 Mount Spurr eruptions and field data

Mount Spurr is an ice-capped, andesitic stratovolcano located 130 km west of Anchorage in the southern part of the Alaska Range. After 10 months of gradually increasing seismic activity, three subplinian eruptions occurred in 1992 at the satellite flank vent of Crater Peak, on June 27, August 18 and September 16-17. Each eruption lasted for 3.5 to 4 hours and generated small volume pyroclastic density currents (PDCs; (Miller et al. 1995)) and eruptive columns rising to ~14 km a.s.l. observed by radar (Rose et al. 2001; Rose et al. 1995). The August and September eruptions were observed in detail (McGimsey et al. 2001; Miller et al. 1995; Rose et al. 2001; Schneider et al. 1995). The August 18 eruption started at 16:42 Alaska Daylight Time (ADT) and waned after 20:00 ADT (Rose et al. 2001). The September event started at 00:03 ADT on the 17th and lasted until ~03:40 ADT (McGimsey et al. 2001; Rose et al. 2001). Satellite infra-

248 red (IR) images indicate that during the 30 to 40 hours following the start of the eruption, the
249 September plume advected downwind more quickly than the August one, with average speeds
250 of 39 and 16 m/s, respectively (Schneider et al. 1995).
251
252 Narrow (30 to 50 km wide) and elongated fallout deposits with DRE volumes of 14 and 15 x
253 10^6 m^3 were produced by the August and September eruptions (McGimsey et al. 2001). The
254 deposits extend towards the east south-east and east north-east, respectively, across the Cook
255 Inlet Basin and the eastern mountain ranges (Chugach and Talkeetna Mountains; Fig. 2). The
256 ASMMs appear at distances greater than 150 km from vent, a distance at which a clear
257 minimum of MpuA is reached (Fig. 2). The proximal deposits contain two types of basaltic
258 andesite clasts – tan and grey pumice – making up a total juvenile content > 90% (Neal et al.
259 1995). Each deposit consists of a lower tephra layer rich in tan pumices (60-80%) comprising
260 more than two thirds of the thickness, and an upper layer dominated by grey pumices (90% in
261 the August deposit and 65% in the September deposit) representing one third of the thickness
262 (Gardner et al. 1998). Tan and grey pumices differ in their density (1.5 ± 0.2 and 2.1 ± 0.3
263 g/cm^3, respectively, for clasts 16-4 mm in size) and their vesicularity (41.7 ± 8.0% and 23.0 ±
264 9.6%; Gardner et al. 1998). Distal ash from site 44 in the August deposit located 265 km from
265 source (Fig. 2) is dominated by particles with 20-40% vesicularity containing plagioclase and
266 pyroxene microlites; smaller microlite-rich glass shards comprise 44% of the studied sample
267 (Riley et al. 2003).
268

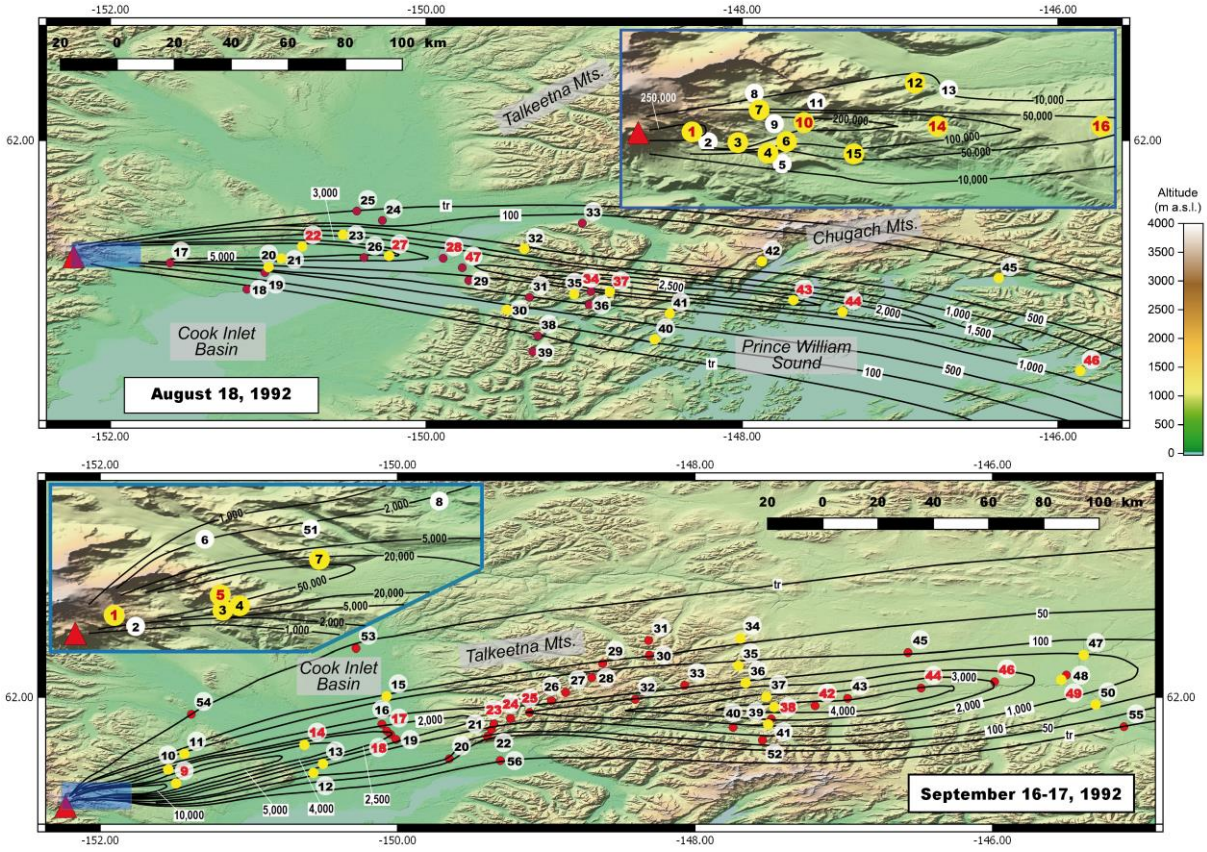

Figure 2: *Maps of the tephra fall deposits from the August 18 and September 16-17, 1992 Mount Spurr eruptions, Alaska, showing the locations where the MpuA of tephra deposited was measured (numbered dots), and the isomass lines (black curves) in g/m² as drawn by the USGS (McGimsey et al. 2001). The yellow dots represent sites where the deposit was also sampled and the grain size measured. The red sample numbers indicate those that we designate as on-axis.*

The MpuA of tephra was carefully measured by USGS researchers throughout the fallout deposits up to 400 km from vent during the week following each eruption (Fig. 2; McGimsey et al. 2001). There were no reports of observations of aggregates falling during the eruptions or preserved within the deposits (McGimsey et al. 2001). The grain size of several samples (27 in the August deposit and 21 in the September deposit, Fig. 2) was analysed by sieving and laser diffraction (McGimsey et al. 2001; Rose et al. 2001; Durant and Rose 2009). We used the grain

size data from McGimsey et al. (2001) and Durant and Rose (2009), except for August sample 44 whose grain size data come from Rose et al. (2001); the grain size distribution reported in Durant and Rose (2009) for this sample is inconsistent with the regional trend and measurements in Rose et al. (2001) and Riley et al. (2003). The TGSDs were reconstructed by Durant and Rose (2009) and are bimodal with fine modes between 3 and 5 Φ (125-32 μm; Fig. 3).

4- Simulation methods

Simulations of individual particle settling

We simulate the sedimentation of individual particles through the atmosphere in the meteorological conditions of the 18 August and 16-17 September 1992 using the theoretical settling scheme of Ganser (1993) for non-spherical particles. This scheme is increasingly applied in numerical models of volcanic plume dispersion and sedimentation, including the model NAME of the London VAAC (e.g., Beckett et al. 2014; Beckett et al. 2015). It is different than the Durant and Rose (2009) model that used a drag coefficient after Brown and Lawler (2003) suitable for spherical particles only.

Here, the particle Reynolds number *(Re)*, drag coefficient *(Cd)* and terminal fall velocity *(Vt)*, are expressed as:

$$Re = \frac{(Vt\ D\ \rho_a)}{\mu_a} \quad (1)$$

$$Cd = \frac{24}{Re\ K_1}\left(1 + 0.1118(Re\ K_1K_2)^{0.6567}\right) + \frac{0.4305\ K_2}{1+\frac{3305}{Re\ K_1K_2}} \quad (2)$$

$$Vt = \left(\frac{4\ g\ D\ (\rho_p - \rho_a)}{3\ Cd\ \rho_a}\right)^{1/2} \quad (3)$$

where D is the particle diameter, ρ_a the density of the atmosphere, μ_a the dynamic viscosity of the atmosphere, and ρ_p the density of the particle. K_1 and K_2 are Ganser's shape factors, defined as:

$$K_1 = \frac{3}{1+2\ \psi^{-0.5}} \quad (4)$$

$$K_2 = 10^{[1.8148\ (-log\psi)^{0.5743}]} \quad (5)$$

where ψ is the 3D sphericity of the particle.

Sedimentation is simulated from the height of plume dispersion (12 km for both eruptions; Neal et al. 1995; Rose et al. 2001), which corresponds roughly to the altitude of the tropopause (Rose et al. 2001). The troposphere is divided into 1 km-thick layers, in which temperature (*T, in Kelvin*), pressure (*P*), ρ_a and μ_a are assumed constant. These parameters are calculated following the International Standard Atmosphere model, using an exact solution to the hydrostatic equation for a column of air, the perfect gas law and the Sutherland law:

$$T = T_0 - L\ h \quad (6)$$

$$P = P_0\ (\frac{T}{T_0})^{5.256} \quad (7)$$

$$\rho_a = \frac{P}{R\ T} \quad (8)$$

$$\mu_a = \frac{1.458\times10^{-6}\, T^{3/2}}{T+110.4} \quad (9)$$

where T_0 and P_0 are the temperature and pressure at sea level (288.2 K and 101.29 x 10^3 Pa, respectively), L is the lapse rate for the troposphere (6.5 K/km), h is the altitude, and R is the gas constant for air (287 $m^2s^{-2}K^{-1}$). Given that *Re* depends on *Vt* and on the air properties, *Re*, *Cd* and *Vt* are calculated iteratively in each atmospheric layer. *Vt* of a particle thus varies with the altitude (Fig. S2C&D in supplementary material). Particles are advected horizontally by the wind (Fig. S2A&B in supplementary material), assuming a constant wind speed and direction in each atmospheric layer and neglecting the vertical component of the wind. Similar to Durant and Rose (2009), we implemented observed horizontal wind data in the simulations using atmospheric soundings collected at Anchorage International Airport at the time closest to the eruption time: 16:00 ADT on August 18 (42 minutes before the start of the August eruption), and 04:00 ADT on September 17, 1992 (4 hours after the start of the September eruption) (Fig. S3 in supplementary material).

We simulate the sedimentation of tan and grey pumices, 16 mm to 4 μm in size, with different values of sphericity (see Fig. S4 in supplementary material for examples of shapes covered by the range of sphericity explored). Based on density profiles observed in many tephra fallout deposits (Bonadonna and Phillips 2003; Cashman and Rust 2016; Eychenne and Pennec 2012), we assume that the density of tan and grey pumices increases linearly with grain size in Φ between Φ = -4 (16 mm), where ρ_p is taken as 1.5 and 2.1 g/cm^3 for tan and grey pumices, respectively, and Φ = 3 (125 μm), where the density reaches the solid density (ρ_p = 2.6 g/cm^3 for both pumice types) and remains constant (Fig. S5 in supplementary material). The threshold grain size for the change in density trend is taken at 125 μm by comparison to the densities of particles from the 2006 Tungurahua fallout deposit (Eychenne and Pennec 2012), which has a

similar composition and microlite content to the Spurr pumices (Wright et al. 2012). The effect of a different density profile has also been explored (see Fig. S5 and S6 in supplementary material).

Mesoscale modelling of the atmospheric wind field

The complex 3D wind field is simulated at the mesoscale with the NCAR Clark-Hall cloud scale model (Clark et al. 1996). This model has been used to simulate fire events (Coen 2013), aircraft-damaging turbulence phenomena (Clark et al. 2000), rainfall development (Thielen et al. 2000), and microphysical processes accompanying cloud seeding (Wobrock et al. 2001). The meteorological model is non-hydrostatic and uses the an-elastic form of the continuity equation. It comprises the prognostic equations for wind field, temperature, water vapour and all forms of cloud/precipitation hydrometeors. A special feature of the model is the use of a terrain-following vertical coordinate, which allows simulation of detailed airflow over complex and steep terrain (Clark 2003). To initialize the model and to force its lateral boundaries, the atmospheric fields of wind, temperature, humidity and pressure were taken from the ECMWF-ERA-interim database for the 18 August and 17 September 1992. The NCAR Clark-Hall cloud scale model accounts for topography-induced buoyancy perturbations of the stratified atmosphere, which can create regions of turbulence in the upper troposphere and lower stratosphere (Eckermann et al. 1999) and alter the wind field locally in the low atmospheric layers (Jiang and Doyle 2004).

5- Results

Grain size and mass variations in the 1992 Mount Spurr fallout deposits

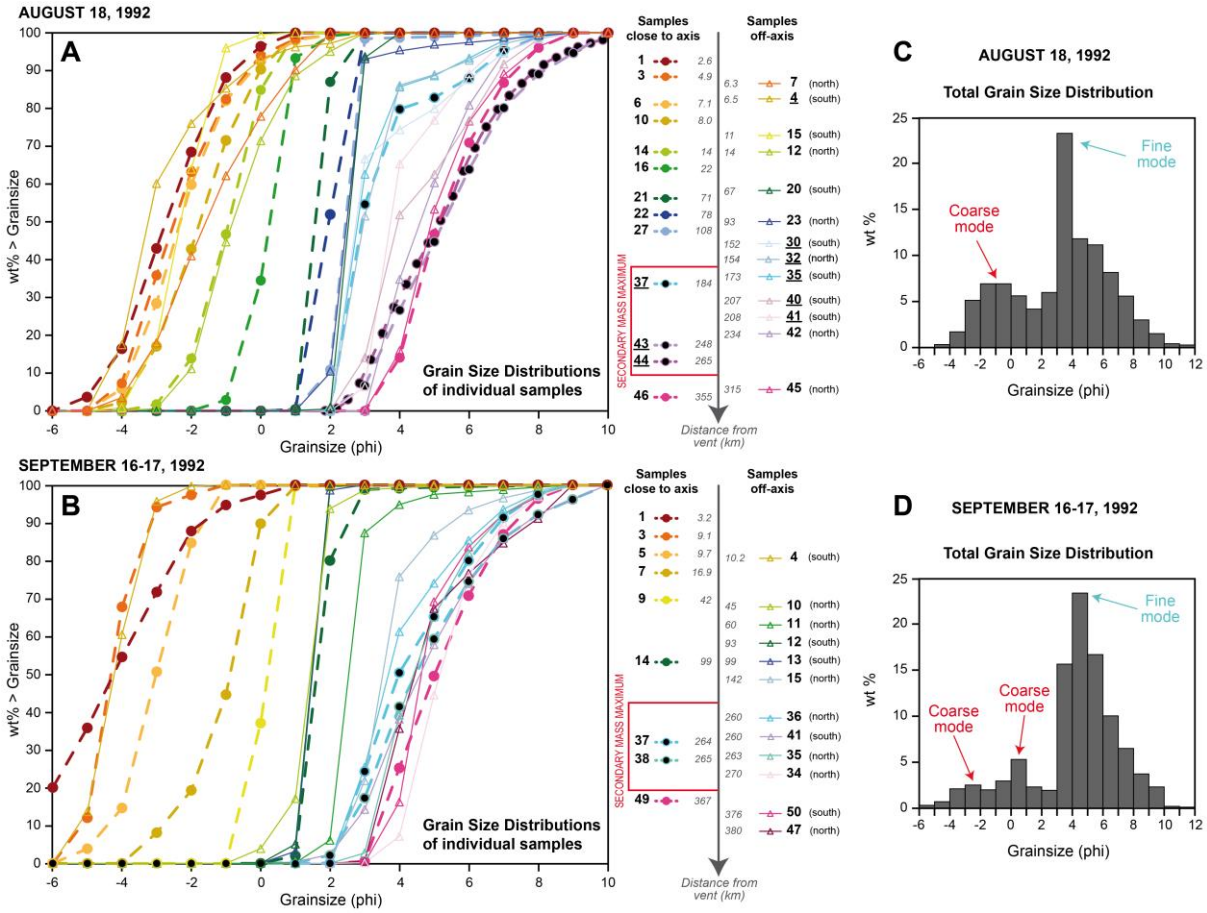

Figure 3: *Cumulative grain size distributions of samples from the August 18* ***(A)*** *and September 16-17, 1992* ***(B)*** *Mount Spurr fallout deposits. The distribution curves are colour coded by their distance from vent (see legends on the right of the plots). The filled and open symbols represent samples located close to- and off the deposit axis, respectively. The samples located in the ASMMs are highlighted by black symbols on the plots. The samples underlined on the right legends have bimodal grain size distributions.* ***(C)*** *&* ***(D)*** *Total Grain Size Distributions of the August 18 and September 16-17, 1992 Mount Spurr fallout deposits, respectively. TGSDs after Durant and Rose (2009).*

The fallout grain size distributions follow similar spatial trends in the August and September deposits (Fig. 3 & 4). The mean size decreases consistently with distance from vent, with the samples close to the deposit axis showing a coarser mean than the off-axis samples (Fig. 4).

The deposit becomes better sorted (the sorting parameter σ decreases) to ~50 km from vent. Samples are extremely well sorted between ~50 and 100 km from vent (Fig. 3 & 4), across the area corresponding to the wide valley of the Cook Inlet Basin (Fig. 2 & 4). Beyond 100 km, σ increases due to an enrichment of the deposit in fine ash (Fig. 4). Individual samples with bimodal grain size distributions are observed in the August deposit (Fig. 3A) at variable distances from vent; they are not restricted to the ASMM. No bimodal samples are observed in the September deposit, where the sampling was sparser. The bimodal distributions are deconvolved as a coarse and a fine subpopulation using DECOLOG 5.0 (Bellotti et al. 2010; Caballero et al. 2014) (Fig. S1 in supplementary material).

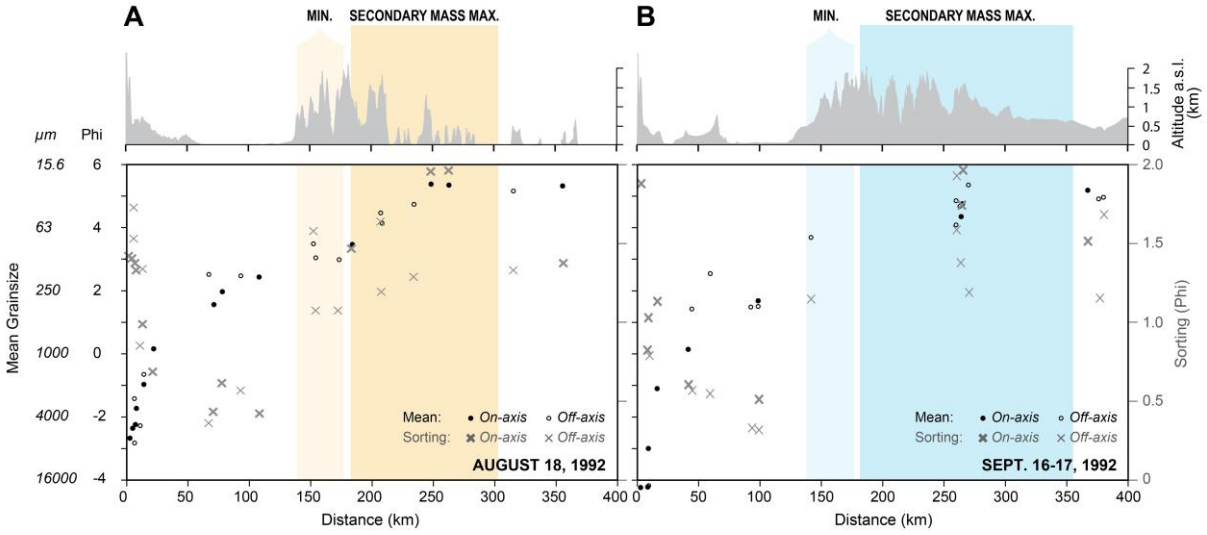

Figure 4: *Variations of the mean (left axis) and sorting (akin to standard deviation; right axis) parameters of the bulk (i.e. non-deconvolved) grain size distributions of samples from the August 18* ***(A)*** *and September 16-17, 1992* ***(B)*** *Mount Spurr fallout deposits. The topography profiles along the deposit axis are represented, and on- and off-axis samples are distinguished. Mean and sorting are defined after Folk and Ward (1957).*

The August and September fallout deposits are characterized by a distal increase in mass with an amplitude of ~2,300 and 3,400 g/m², respectively, corresponding to the ASMMs (Fig. 5).

After reaching a minimum 140 to 160 km from vent in the August deposit and 140 to 170 km from vent in September, the MpuA attains a secondary maximum between 170 and 300 km from vent in the August deposit, and between 180 and 350 km from vent in September. In both deposits, the mass minimum occurs across the windward flank of a 2 km-high mountain range (Chugach and Talkeetna Mountains; Fig. 2), while the maximum spreads across the leeward flank (Fig. 5A & 5B).

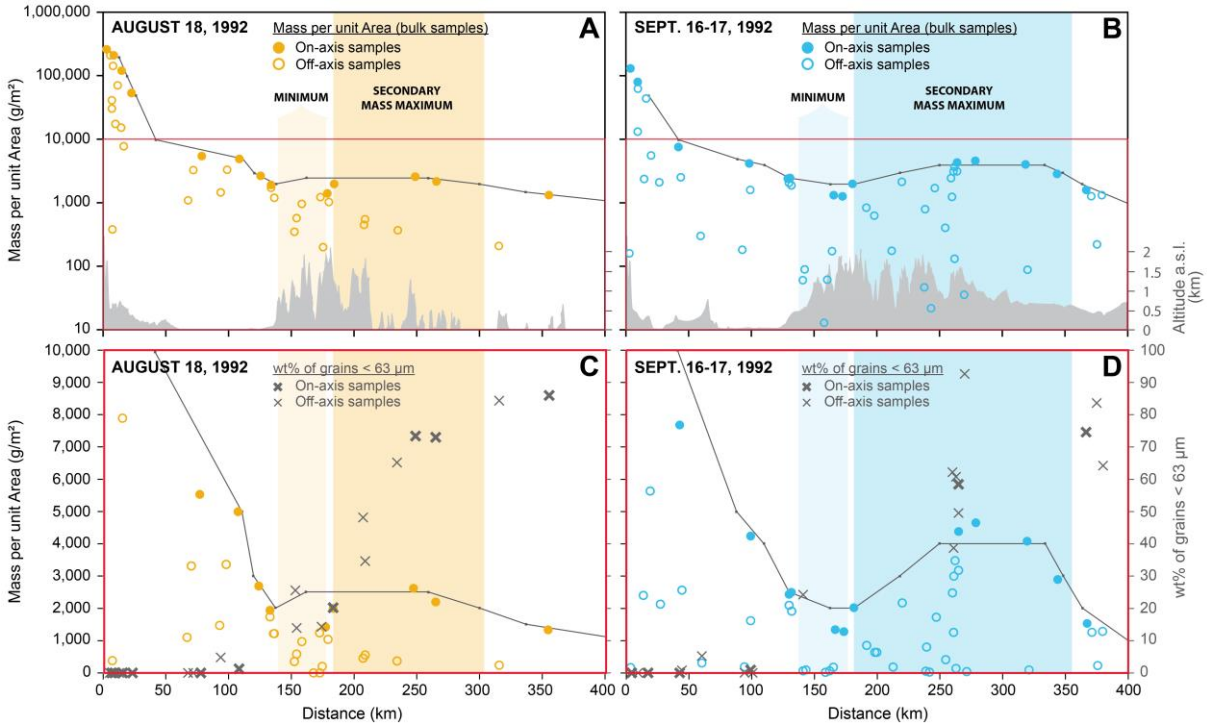

Figure 5: *Variation of MpuA with distance from vent, within the August 18* ***(A & C)*** *and September 16-17, 1992* ***(B & D)*** *Mount Spurr fallout deposits. The topography profiles along the deposit axes are represented in* ***(A & B)****.* ***(C & D)*** *are expanded plots (red boxes) of* ***(A & B)****, and represent the proportion of fine ash (grains finer than 63 µm) on the right axis (grey crosses). Minima and maxima in the MpuA profiles are highlighted in the plots and determined from the on-axis MpuA variations, with the minima and maxima taken as the areas where MpuA < 1500 g/m² and MpuA > 2000 g/m², respectively. The thin grey lines represent the along the*

axis linear interpolation of the isomass lines as drawn by McGimsey et al. (2001) and represented in Fig. 2.

The fallout deposits lack fine ash (< 63 μm) to ≤140 km from vent (Fig. 5C & D), a distance that corresponds to the foothills of the Chugach and Talkeetna Mountain ranges, where fine ash is first found on the ground. Beyond this location, the proportion of fine ash increases steadily (although with some scatter) with distance, across both the local minima and the ASMMs (Fig. 5C & D). The proportion of ash <125 μm follows the same trend as the fine ash (< 63 μm; Fig. 6) and is thus not spatially correlated with the MpuA variations or ASMMs. The proportion of ash < 63 μm starts to increase just before the local mass minima, about 100 km closer to the vent than the ASMMs. While MpuA decreases away from the ASMMs (both downwind and crosswind), the proportion of ash < 63 μm (and < 125 μm) keeps increasing downwind, with no systematic crosswind trend. This indicates that the distal increase in sedimentation causing the ASMMs does not result from preferential settling of ash < 63 μm (or < 125 μm) compared to coarser grain sizes, in contrast to predictions of aggregation models for ASMM formation (see section 2 and Fig. 1B).

Settling behaviour of individual particles

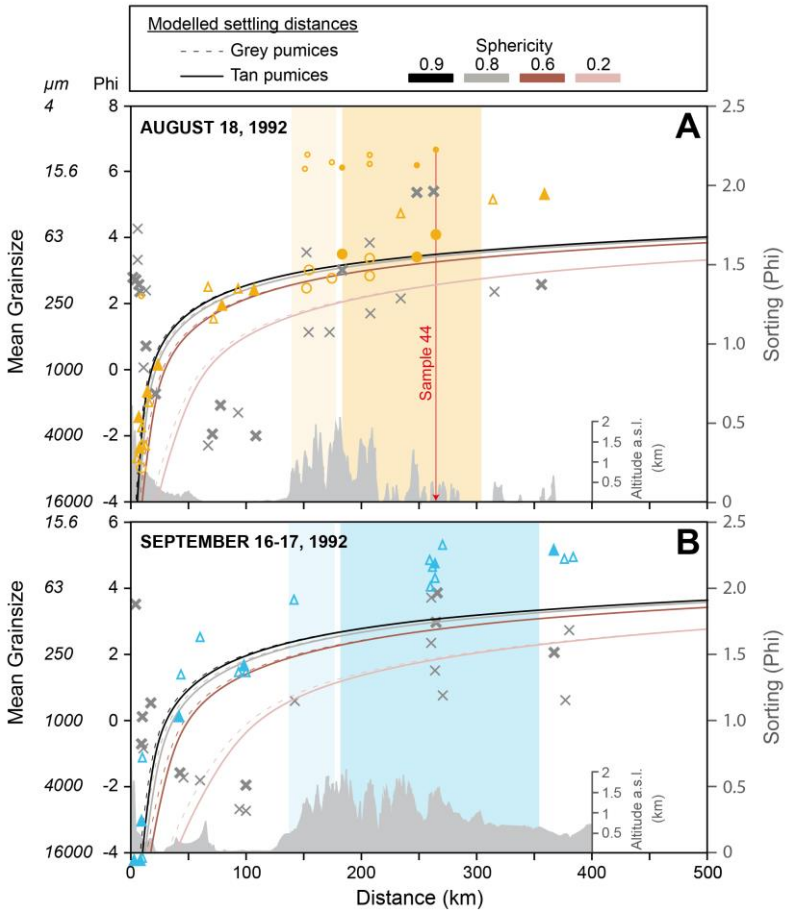

446

447 ***Figure 6:*** *Comparison of simulated vs. observed grain size variation in the August 18* ***(A)*** *and*
448 *September 16-17, 1992* ***(B)*** *Mount Spurr fallout deposits. The mean (after Folk and Ward*
449 *(1957)) of unimodal samples (triangles), as well as coarse (circles) and fine subpopulations*
450 *(dots) deconvolved from the bimodal distributions, are represented. The on-axis samples (Fig.*
451 *2) are represented as closed symbols. The curves represent the settling distances of individual*
452 *particles of various shapes in the local wind field at the time of the eruptions, for tan*
453 *(continuous lines) and grey pumices (dashed lines). The grey crosses represent the proportion*
454 *of ash < 125 μm in size (right axis), with on-axis samples as bold crosses. The topography*
455 *profiles along the deposit axes are represented, as well as the secondary minima and maxima*
456 *in mass (same representation as in Fig. 5).*

457

For sphericity values ranging from 0.9 to 0.6, the settling model for individual particles reproduces the mean of the unimodal grain size distributions over the first 100 km of the fallout deposits (Fig. 6). The density difference between tan and grey pumices makes relatively little difference to the modelled deposition. A break-in-slope in the grain size trend with distance is observed at ~50 km from vent in both the field and modelled data. The absence of fine ash on the ground in this area is consistent with this model prediction. In the August deposit, the settling model also explains the coarse subpopulations of the bimodal samples between 100 and 250 km from vent (Fig. 6A). The fine ash observed in the deposits (as part of a fine subpopulation in the August bimodal distributions, or as part of the unimodal distributions), in contrast, appears much closer to the vent than model predictions for non-spherical particles (Fig. 6), concurring with the findings of Durant and Rose (2009) based on spherical particles. Our simple modelling approach does not account for turbulence and mesoscale motions that would help the finest particles to travel even further (Beckett et al. 2015). Although the scarcity of grain size data in the September deposit (Fig. 6B) makes it more difficult to assess the capacity of the model to reproduce the field data, we can safely infer that, as with the August case, the model of individual particle settling explains well the field sedimentation pattern for grains larger than ~100 μm.

3D atmospheric wind field

The wind fields modelled by our mesoscale simulations of the atmosphere during the August and September Spurr eruptions reveal complex 3D patterns (Fig. 7; Fig. S9 in supplementary material). The wind field is strongly affected by topography, with strong vertical oscillations generated by the steep topographic variations characteristic of the mountainous regions of Alaska (Fig. 7A & B). The vertical oscillations propagate to the stratosphere, creating a highly turbulent troposphere mostly located above the topography. Between 2 and 4 km a.s.l., the

483 horizontal wind field is also variable, with wind channelled towards the north and north-East in
484 the Cook Inlet Basin, and a decrease of the wind speed in the basin west of the Talkeetna
485 mountains (Fig. 7C-F). The September wind field (Fig. 7B, D & F) is characterized by higher
486 velocities (both vertical and horizontal) than in August, which produces a more turbulent
487 atmosphere. Strong contrasts in horizontal wind velocities in the low troposphere (2 to 4 km
488 a.s.l.) are manifested as moderate winds in the Cook Inlet Basin and stagnant areas on the lee
489 side of the Talkeetna mountains (Fig. 7B & D).
490

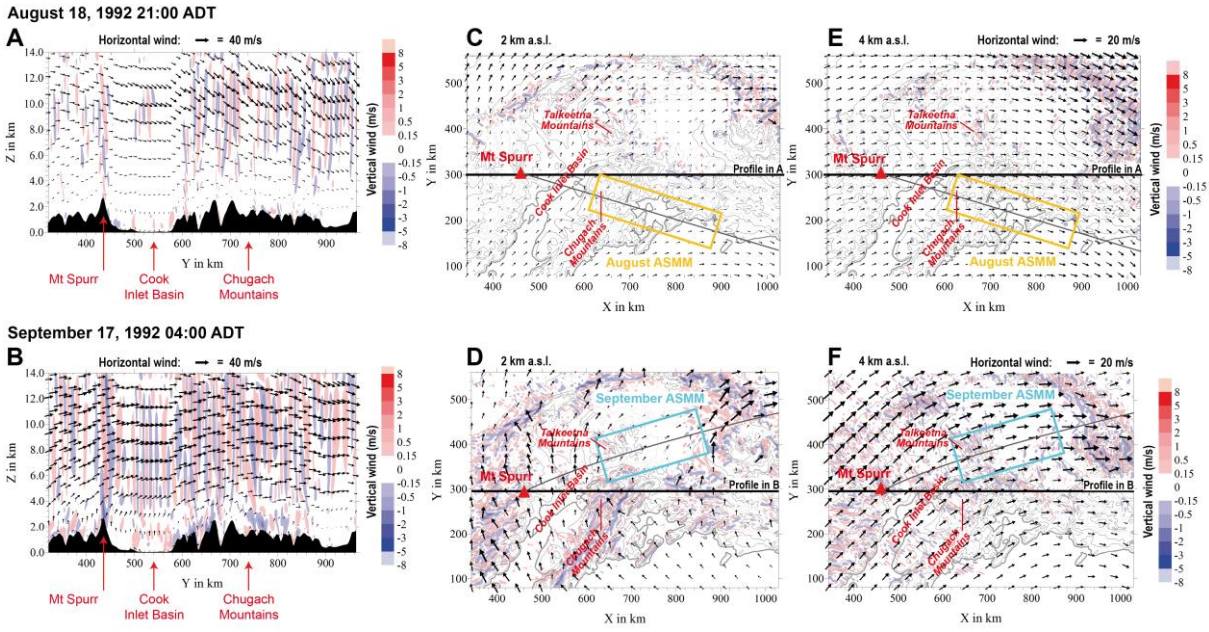

491

492 ***Figure 7:*** *Horizontal (arrows) and vertical (coloured areas) wind patterns in the Alaska region*
493 *downwind of Mount Spurr on August 18 and September 17, 1992, about 4 hours after the*
494 *eruptions started. The wind field is simulated at the mesoscale with the NCAR Clark-Hall cloud*
495 *scale model (Clark et al. 1996) using meteorological data from the ECMWF-ERA-interim*
496 *database.* ***(A & B)*** *Vertical profiles along a west to east cross section through the mountains.*
497 ***(C & D)*** *Maps of the wind pattern at 2 km a.s.l.* ***(E & F)*** *Maps of the wind pattern at 4 km a.s.l.*
498 *The arrow length and direction represent the speed and xy direction of the horizontal*
499 *component of the wind, respectively. The vertical component of the wind is colour-coded (see*

*legend), with positive and negative velocities corresponding to upward and downward winds, respectively. The scales for vertical and horizontal wind velocities are the same in **(C, D)** than **(E, F)**. The black and grey lines in **(C, D, E & F)** represent the East-West traverse represented in profiles **(A & B)**, and the plume trajectories, respectively. Additional maps representing the wind field at 6 and 8 km a.s.l. are presented in Fig. S9 of Supplementary Material.*

6- Discussion

Sedimentation behaviour during the Mount Spurr eruptions

The results of our individual particle settling simulations show that during the Mount Spurr eruptions, ash coarser than 100 µm settled predominantly as individual grains (Fig. 6) and was progressively depleted from the plume, leading to an increased proportion of fine ash depositing with distance (Fig. 3, 5 & 6). A different type of settling mechanism appears to control the sedimentation of fine ash, which reached the ground much closer to the vent than predicted by individual particle settling (Fig. 6), as has been documented in a number of other fallout deposits (e.g., Brazier et al. 1983; Engwell and Eychenne 2016; Rose and Durant 2009). As discussed above, numerous processes can explain the observed accelerated transfer of fine ash towards the ground, including aggregation (e.g., Brown et al. 2012; Rose and Durant 2011; Taddeucci et al. 2011; Van Eaton et al. 2012) and other collective sedimentation behaviours such as en-masse settling in convective instabilities (Carazzo and Jellinek 2012; Manzella et al. 2015), hydrometeor-enhanced sedimentation (Durant and Rose 2009; Durant et al. 2009) and entrainment of fine ash in the wake of settling coarser grains (Del Bello et al. 2017; Di Muro et al. 2008; Eychenne et al. 2015; Lovell and Rose 1991). But does the accelerated sedimentation of fine ash cause the formation of the ASMMs in the Spurr fallout deposits?

To answer this question we compare the simplified depositional patterns illustrated in Figure 1 to observations of mass and grain size distributions in the two Spurr deposits. Importantly, there is no apparent correlation between mass and proportion of fine ash within the Spurr ASMMs (Fig. 5 & 6), as would be expected if a size-selective sedimentation process (i.e. enhancing preferentially the settling of fine ash) had caused the distal deposition increase (see section 2 and Fig. 1B). Instead, we observe a gradual enrichment in fine ash with distance that initiates just before the mass minima and continues beyond the ASMMs, which reflect a local MpuA increase (Fig. 5 & 6). These data suggest that the mechanism responsible for the increased settling affected the sedimentation of both fine ash and coarser particles in a way that modulated the distance and rate at which all the suspended material reached the ground (Fig. 4 & 5). We thus conclude that while enhanced fine ash sedimentation processes might have been occurring during the Spurr eruptions, we find no evidence that they produced aggregates with a unique set of characteristics that would have been necessary to trigger the ASMM formation. To constrain the origin(s) of the ASMM and explain the observed decoupling of MpuA and proportion of fine ash, we explore alternative processes affecting particle sedimentation, including (1) changes in horizontal wind velocity at the tropopause during the course of the eruption, (2) the heterogeneity of particle size, shape and density documented within the ASMM, (3) the bimodality of the source grain size, and (4) complex 3D wind patterns related to topography-induced perturbations.

Effect of horizontal wind variations

Fallout deposits represent accumulation of material integrated over the duration of tephra emission. Atmospheric conditions change through time, and can thus modify the settling distance of similar material (settling velocity) emitted at different times. This alone can complicate the lateral mass variations of fallout deposits.

Satellite images of downwind spreading of the August plume show that during the first 40 hours of dispersion, the plume front travelled more than 2000 km at an average speed of 16 m/s (Schneider et al. 1995). The detached plume passed over the sampling area (~400 km extent) in less than 20 hours (Schneider et al. 1995). The elongated and narrow shape of the fallout deposit (Fig. 2) suggests a high wind speed at the altitude of dispersion. A high velocity layer (25 to 27 m/s) was located at an altitude of about 11 km a.s.l. at 16:00 ADT on August 18 (42 minutes before the eruption started; Fig. S3 in supplementary material). It weakened (to 14-16 m/s) but persisted to 04:00 ADT on the morning of the 19th (~11 hours after the eruption started), and strengthened again (to 20-25 m/s) by 16:00 ADT on the same day (~23 hours after the eruption started). Simulations using the weakest wind profile (04:00 ADT on August 19) show a significant impact of wind changes on particles finer than 63 μm (Fig. S7 in supplementary material). Compared to transport in the August 18 16:00 ADT wind field, 63 μm and 30 μm individual particles would settle ~60 and 250 km closer to the vent, respectively, at the lower wind speeds (Fig. S7 in supplementary material). At 21:11 ADT, ~4.5 hours after the eruption started and ~1 hour after it stopped, satellite infra-red (IR) images show a plume still connected to the vent extending ~400 km toward the south-east, with an optically opaque core indicating high particle concentrations and/or presence of material coarser than 15 μm in diameter (Rose et al. 2001; Schneider et al. 1995). This indicates that substantial deposition must have occurred while the winds weakened, which could explain some of the fine ash within the depositional area.

To explore whether the change in wind velocity could have produced the ASMM, we add observations from September, which also occurred at the time of a high velocity wind layer. The wind speed averaged 37 m/s at an altitude of about 12 km at 04:00 ADT on the 17th (~4

hours after the eruption started); by 16:00 ADT on the same day (~16 hours after the eruption started) wind speeds persisted at 30 m/s but at altitudes that decreased 10 to 12 km (Fig. S3 in supplementary material). The plume front ultimately travelled more than 3500 km at an average speed of 39 m/s and the detached plume passed over the sampling area in less than 10 hours (Schneider et al. 1995). We assume that such small wind changes had very little effect on the transport of the September plume within the depositional area, and cannot explain the formation of the ASMM in this deposit. From this we conclude that the August ASMM may also require additional depositional mechanism(s).

Effect of particle characteristics

Pyroclasts transported in volcanic plumes are more texturally and morphologically complex than depicted in our settling model, which could affect the distal sedimentation pattern. Fully characterising the diversity of texture and shape in a tephra sample, and determining the effect of these variations on the settling behaviour of the particles, is challenging. Riley et al. (2003) proposed an original approach by measuring, in the laboratory, the settling velocity (*Vt*) of particles from August sample 44 (Rose et al. 2001; Riley et al. 2003), which was collected on-axis at a distance of 265 km from vent in Wells Bay, that is, at the distal end of the ASMM (Fig. 2, 3 & 6). They used a Roller air elutriation device, which sorts particles into *Vt* groups by modulating the air flow rate injected in a tube holding the sample. Riley et al. (2003) distinguished vesicular from dense grains, and measured the size and shape of representative grains in each *Vt* group (Fig. 8A).

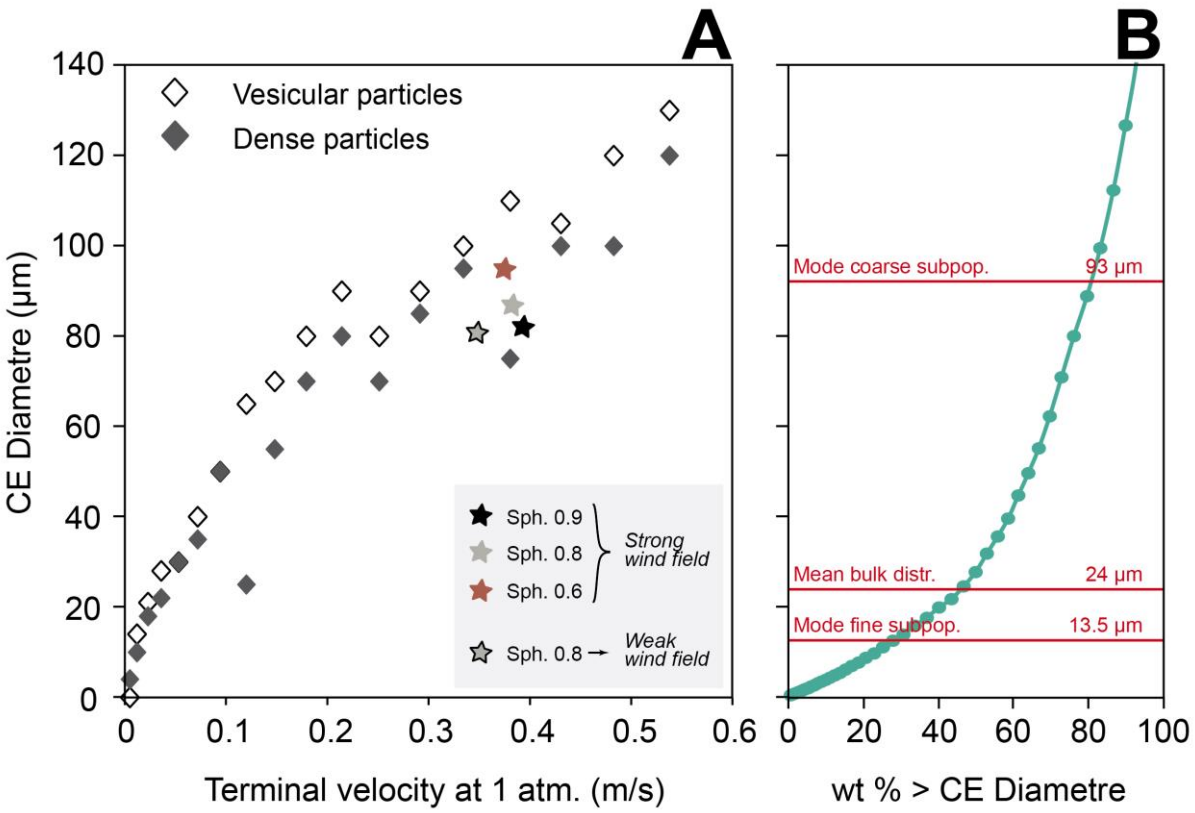

Figure 8: (A) *Mean Circle Equivalent (CE) Diameter of dense (filled diamonds) and vesicular particles (open diamonds) measured in the Vt groups identified within tephra sample 44 (Fig. 2) of the August 18, 1992 Mount Spurr fallout deposit (data after Riley et al. (2003)). The stars represent theoretical Vt at sea level (equivalent conditions to the laboratory) for the particles predicted to reach the ground at the location of sample 44 (265 km from vent) by our individual particle settling scheme for different sphericity values in the strong wind field of August 18 16:00 ADT. For a sphericity of 0.8, Vt at sea level was also recalculated for particles expected to reach the location of sample 44 in a weak wind field (August 19 04:00 ADT wind profile; see Fig. S3).* ***(B)*** *Cumulative grain size distribution of sample 44 (after Rose et al. 2001), including the mean of the bulk grain size distribution, and the modes of the coarse and fine subpopulations (Fig. S1 in supplementary material).*

The *Vt*s measured in sample 44 span a wide range of velocities corresponding to particles ranging from 4 to 130 µm in size (measured as circle-equivalent diameter CE; Fig. 8). Overall,

612 vesicular particles have lower *Vts* than dense ones without an obvious link to their shape (see
613 measurements of 2D roughness and sphericity in Fig. S8 in supplementary material). Our
614 settling simulations using the August 18 16:00 ADT wind field predict that vesicle-free particles
615 85-100 μm in size (depending on the sphericity) would reach the ground at the location of
616 sample 44 if they were falling individually (Fig. 6). We calculated *Vt* for these particles in sea
617 level atmospheric conditions (comparable to *Vt* measured in the laboratory), which is ~0.4 m/s
618 (Fig. 8A). According to theory, particles with $Vt > 0.4$ m/s should have settled closer to the
619 vent, while particles with $Vt < 0.4$ m/s should have settled further away. The predominant grain
620 size mode at ~100 μm (coarse grain size mode in Fig. 8B) is consistent with the grain sizes
621 expected to reach this distance as individual particles (Fig. 8A), especially when considering
622 variations in sphericity (Fig. 8A) and particle density (Fig. S6). Settling of particles in the grain
623 size distribution mass-based mean (Folk and Ward 1957) at ~24 μm requires accelerated
624 sedimentation, which cannot be explained by changes in wind speed through time (see modelled
625 *Vt* for sphericity 0.8 in the August 19 04:00 ADT weak wind field in Fig. 8A). These findings
626 are consistent with the conclusions drawn from Figure 6, which show that individual settling
627 can explain only the sedimentation behaviour of particles ≥ 100 μm. Below this threshold, the
628 settling location of the particles is not controlled by the *Vt* of individual grains, from which we
629 conclude that their size, shape and texture did not play a primary role in the sedimentation
630 process.
631
632 *Effect of the bimodality of the source grain size*
633 While only a limited number of individual tephra samples show bimodality (Fig. 3 & S1 in
634 supplementary material), the TGSDs of both the August and September Mount Spurr fallout
635 deposits are polymodal (Durant and Rose 2009). The August TGSD has a coarse mode between
636 4 and 1 mm and a fine mode at 125 μm (Fig. 3C), while the September TGSD has two coarse

637 modes at 8 and 1 mm, and a fine mode at 63 μm (Fig. 3D). The coarse modes comprise grain
638 sizes found within the first 50 km of the deposits (Fig. 6). The fine mode of the August TGSD
639 corresponds to the mean of the coarse grain size subpopulation found in the August ASMM,
640 while the fine mode of the September TGSD corresponds to the mean of the unimodal grain
641 size distributions found in the September ASMM (Fig. 6). This suggests that the increased
642 sedimentation at the ASMMs could have been generated, at least in part, by an over-
643 representation of some grain sizes in the plume (i.e. the fine modes of the TGSDs). This could
644 explain why the numerical simulations of the September eruption by Folch et al. (2010)
645 produced an ASMM at about the right location without including aggregation. It is important
646 to note, however, that TGSDs are reconstructed by weighting individual grain size distributions
647 by the mass of tephra deposited close by (Durant and Rose 2009). Consequently, local increases
648 of MpuA that generate ASMMs may produce TGSD with an artificial over-representation of
649 the grain sizes found in the ASMMs. That said, the distribution of sampling sites of the Spurr
650 deposits (Fig. 2) extends well outside of the ASMMs, and thus supports the idea that the erupted
651 TGSD, particularly the location and magnitude of the fine mode, should be considered in
652 models of ash sedimentation.
653
654 The importance of the TGSD for tephra dispersion and sedimentation underlines the importance
655 of understanding the mechanisms that generate polymodal source grain size distributions. At
656 Spurr, the origin of the bimodality of the TGSD is not known. The fine modes are often related
657 to a secondary process of fragmentation, such as comminution in pyroclastic density currents
658 (PDCs; Bernard and Le Pennec 2016; Jones et al. 2016), which can produce significant fine ash
659 enrichment in some fallout deposits (Bonadonna et al. 2002; Eychenne et al. 2015; Eychenne
660 et al. 2012). The August and September eruptions, however, produced only small-volume PDCs
661 (< 3 km runout distances; Miller et al. 1995), and are thus unlikely sources of abundant fine

ash. Another possibility is fine ash production by particle attrition during transport in the volcano conduit and the eruptive column, which can also generate a fine peak in TGSDs (Jones and Russell 2017). We would expect attrition to create particles with sizes that are commensurate with textural heterogeneities of the pumice. The fine modes do not correspond, however, to the sizes of the phenocrysts or the microlites observed within lapilli and ash (Gardner et al. 1998; Riley et al. 2003), although the presence of two distinct pumice types (with varying crystallinity and vesicularity) suggests that the polymodality may arise from heterogeneities in the erupted magma. Additionally, seismicity accompanying the Spurr eruptions suggests relatively deep magma storage (~10 km; Roman et al. 2004), and consequently the potential for protracted post-fragmentation magma transport within the conduit.

Effect of topography on atmospheric circulations

The locations of the Spurr ASMMs appear to be correlated with topography, with the local minima occurring on the windward flank of 2 km-high mountain ranges and the maxima spreading across the leeward flank (Chugach Mountains in the August deposit and Talkeetna Mountains in September; Fig. 2, 5A & 5B). Directly upwind of both mountain ranges is the Cook Inlet Basin, where all tephra samples are extremely well sorted and lack particles finer than 125 μm (Fig. 4 & 6). Sedimentation of fine ash starts at the foothills of the mountains (Fig. 5), despite higher horizontal wind velocities in September than in August (Fig. S3). These findings suggest a relationship between ash deposition and topography.

The mesoscale models of the atmospheric wind field (Fig. 7; Fig. S9 in supplementary material) highlights the importance of topography-induced atmospheric flow perturbations on the formation of ASMMs during the 1992 Spurr eruptions. Resulting vertical wind velocities of >

687 1m/s are significantly larger than *Vt*s of particles <100 μm (Fig. 7); *Vt* measurements in sample
688 44 show that particles smaller than 140 μm have *Vt* < 0.6 m/s (Fig. 8). This comparison suggests
689 that these vertical wind variations can affect tephra settling. Along both plume trajectories (Fig.
690 7C,D,E&F and Fig. S9 in supplementary material), the strongest oscillations of the vertical
691 wind component are located above the complex topography of the mountain ranges. Such
692 oscillations generate turbulence in the troposphere that can promote particle mixing and
693 electrostatic aggregation of ash (Schumacher and Schmincke 1995). Turbulence can also
694 increase the *Vt* of individual small particles as a result of the effect of inertia on the interaction
695 of the particles with turbulence in an ambient flow (Maxey and Corrsin 1986; Maxey 1987).
696 These oscillations are stronger in more rapid wind fields (see August vs. September vertical
697 wind field; Fig. 7). Efficient mixing may also aid hydrometeor development and facilitate en-
698 masse sedimentation due to hydrometeor sublimation (Durant and Rose 2009). It can also
699 promote entrainment of fine particles in the wakes of coarser grains (Lovell and Rose 1991),
700 and development of gravitational instabilities by maintaining concentrated clouds with limited
701 sedimentation until they collapse and settle all particle sizes in particle-rich fingers (Carazzo
702 and Jellinek 2013). The correlation between the locations of these highly turbulent atmospheric
703 zones (in relation to topography) and the location of enhanced deposition on the ground
704 suggests that such processes were possible, and helps to explain the wide range of particle sizes
705 and *Vt*s found in the ASMMs (Fig. 7; Fig. S9 C & D in supplementary material).
706
707 We conclude that topographically-generated turbulence can accelerate the transfer of particles
708 towards the low atmospheric layers (by mechanisms that include but are not limited to
709 aggregation), where particle suspension or deposition is then strongly controlled by the
710 atmospheric circulations. In fact, we note that 3D simulations of the September plume
711 dispersion and sedimentation (Folch et al. 2010) defined the atmosphere with a WRF model

712 that accounts for complex topography, and therefore that topographic effects may have added
713 to the effects of the bimodal TGSD to produce the ASMM, even without aggregation.
714
715 **7- Conclusion**
716
717 The crosswind and downwind variations of mass and grain size within the 1992 August and
718 September Mount Spurr fallout deposits indicate that the ASMMs did not result from
719 preferential settling of fine (<100 μm) ash relative to coarser grain sizes. Moreover, aggregation
720 processes usually invoked to explain the formation of ASMMs cannot satisfactorily explain
721 their occurrence in the Spurr deposits. Simulations of individual but non-spherical particle
722 settling through a homogeneous and horizontally stratified atmosphere indicates that enhanced
723 settling at ASMMs affected the sedimentation of both fine ash and coarser particles. We show
724 that the temporal variations of the wind field during eruption are not sufficient to generate the
725 ASMMs. Measurement of the particle fall velocities in a sample from the August deposit shows
726 that the texture and morphology of the particles had only a minor effect on settling within the
727 ASMM. In contrast, the bimodality of the source grain size could have produced the ASMMs,
728 as the fine modes correspond to the grain sizes found at these locations. We also observe a link
729 between the deposit characteristics and the topography: in both deposits, the mass local
730 minimum occurs across the windward flank of a 2 km-high mountain range, while the local
731 maximum (i.e. the ASMM) spreads across the leeward flank; both deposits also exhibit a change
732 in sorting characteristics across the mountains. Mesoscale models of the three-dimensional
733 wind field highlight the oscillations of the vertical wind field caused by topography; these
734 oscillations can promote particle mixing, aggregation, and aid formation of hydrometeors, and
735 resulting deposition via gravitational instabilities and by wake capture.
736

737 Importantly, this work shows that the formation of ASMMs is not always directly related to
738 processes of enhanced sedimentation of fine ash. The pronounced Spurr ASMMs are likely the
739 consequence of a combination of factors, including the original polymodality of the TGSD and
740 enhanced tephra sedimentation due to topography-induced perturbations of the wind field. Such
741 topography effects may also play an important role in the formation and longevity of ash-
742 hydrometeors, and should be explored in relation to en-masse sedimentation processes of
743 volcanic plumes due to hydrometeor sublimation (Durant and Rose 2009; Durant et al. 2009).
744 This work also highlights that using mass distributions in ASMMs to constrain aggregation
745 processes without considering grain size characteristics (e.g., Folch et al. 2010; Mastin et al.
746 2016) may limit our understanding of the ensemble of processes that likely control ash
747 sedimentation. We finally stress the value of combining particle transport modelling with
748 detailed deposit observations, including not only mass depositional patterns on the ground but
749 also detailed studies of grain shape, size, density and, importantly, direct measurement of *Vt*s.
750 Finally, we emphasize that including grain size – and not solely the mass – model evaluation
751 of fallout deposits is necessary to fully assess the quality of the sedimentation scheme. Recent
752 modelling work has shown that such approach reduces the uncertainty on the simulation results
753 (White et al. 2017).
754
755 **Acknowledgements**
756 J. Eychenne was funded by K. Cashman's AXA Research Fund and by a fellowship from the
757 French National Research Institute for Sustainable Development (IRD). We thank Adam
758 Durant and Game McGimsey for providing us with raw field and grain size data. We also thank
759 Game McGimsey for providing information on the sampling campaigns and observations made
760 in the field regarding aggregation. We thank editor Michael Poland and two anonymous
761 reviewers for detailed and constructive comments that greatly improved the quality of the

762 manuscript. Data presented in this work are fully available in the main text and in Supporting
763 Information.
764
765 **References**
766 Alfano F, Bonadonna C, Delmelle P, Costantini L (2011) Insights on tephra settling velocity
767 from morphological observations. Journal of Volcanology and Geothermal Research
768 208(3–4):86-98
769 Bagheri G, Rossi E, Biass S, Bonadonna C (2016) Timing and nature of volcanic particle
770 clusters based on field and numerical investigations. Journal of Volcanology and
771 Geothermal Research 327:520-530
772 Beckett FM, Witham CS, Hort M, Stevenson JA, Bonadonna C, S.C. M (2014) The sensitivity
773 of NAME forecasts of the transport of volcanic ash clouds to the physical characteristics
774 assigned to the particles. UK Met Office Forecasting Research Technical Report 592
775 Beckett FM, Witham CS, Hort MC, Stevenson JA, Bonadonna C, Millington SC (2015)
776 Sensitivity of dispersion model forecasts of volcanic ash clouds to the physical
777 characteristics of the particles. Journal of Geophysical Research: Atmospheres 120:
778 11,636–11,652
779 Bellotti F, Capra L, Sarocchi D, D'Antonio M (2010) Geostatistics and multivariate analysis as
780 a tool to characterize volcaniclastic deposits: Application to Nevado de Toluca volcano,
781 Mexico. Journal of Volcanology and Geothermal Research 191(1-2):117-128
782 Bernard J, Le Pennec J-L (2016) The milling factory: Componentry-dependent fragmentation
783 and fines production in pyroclastic flows. Geology 44(11):907-910
784 Bonadonna C, Mayberry GC, Calder ES, Sparks RSJ, Choux C, Jackson P, Lejeune AM,
785 Loughlin SC, Norton GE, Rose WI, Ryan G, Young SR (2002) Tephra fallout in the

786 eruption of Soufriere Hills Volcano, Montserrat. Geological Society, London, Memoirs
787 21(1):483-516
788 Bonadonna C, Phillips JC (2003) Sedimentation from strong volcanic plumes. J. Geophys. Res.
789 108(B7):2340
790 Brazier S, Sparks RSJ, Carey SN, Sigurdsson H, Westgate JA (1983) Bimodal grain size
791 distribution and secondary thickening in air-fall ash layers. Nature 301:115-119
792 Brown PP, Lawler DF (2003) Sphere drag and settling velocity revisited. Journal of
793 Environmental Engineering-Asce 129(3):222-231
794 Brown RJ, Bonadonna C, Durant AJ (2012) A review of volcanic ash aggregation. Physics and
795 Chemistry of the Earth, Parts A/B/C 45-46:65-78
796 Bursik MI, Sparks RSJ, Gilbert JS, Carey SN (1992) Sedimentation of tephra by volcanic
797 plumes: I. Theory and its comparison with a study of the Fogo A plinian deposit, Sao
798 Miguel (Azores). Bulletin of Volcanology 54(4):329-344
799 Caballero L, Sarocchi D, Soto E, Borselli L (2014) Rheological changes induced by clast
800 fragmentation in debris flows. Journal of Geophysical Research: Earth Surface
801 119(9):2013JF002942
802 Carazzo G, Jellinek AM (2012) A new view of the dynamics, stability and longevity of volcanic
803 clouds. Earth and Planetary Science Letters 325–326(0):39-51
804 Carazzo G, Jellinek AM (2013) Particle sedimentation and diffusive convection in volcanic
805 ash-clouds. Journal of Geophysical Research: Solid Earth 118:1-18
806 Carey SN, Sigurdsson H (1982) Influence of particle aggregation on deposition of distal tephra
807 from the May 18, 1980, eruption of Mount st. Helens volcano. Journal of Geophysical
808 Research 87(B8):7061-7072

809 Cashman K, Rust A (2016) Volcanic ash – generation and spatial variations In: Mackie S,
810 Ricketts H, Watson M, Cashman K, Rust A (eds) Volcanic ash: hazard observation.
811 Elsevier,
812 Clark TL (2003) Block-Iterative Method of Solving the Non-hydrostatic Pressure in Terrain-
813 Following Coordinates: Two-Level Pressure and Truncation Error Analysis. J. Appl.
814 Meteor. 42:970-983
815 Clark TL, Hall WD, Coen JL (1996) Source code documentation for the Clark-Hall Cloud-scale
816 model: Code version G3CH01. In: The National Center for Atmospheric Research
817 (NCAR) Technical Note. p 174
818 Clark TL, Hall WD, Kerr RM, Middleton D, Radke L, Ralph FM, Neiman PJ, Levinson D
819 (2000) Origins of Aircraft-Damaging Clear-Air Turbulence during the 9 December 1992
820 Colorado Downslope Windstorm: Numerical Simulations and Comparison with
821 Observations. Journal of the Atmospheric Sciences 57(8):1105-1131
822 Coen JL (2013) Modeling Wildland Fires: a description of the coupled atmosphere-Wildland
823 Fire environment model (CAWFE). In: NCAR Thecnical Notes.
824 Cornell W, Carey S, Sigurdsson H (1983) Computer simulation of transport and deposition of
825 the campanian Y-5 ash. Journal of Volcanology and Geothermal Research 17(1–4):89-
826 109
827 Costa A, Folch A, Macedonio G (2010) A model for wet aggregation of ash particles in volcanic
828 plumes and clouds: 1. Theoretical formulation. Journal of Geophysical Research 115(B9)
829 Del Bello E, Taddeucci J, de' Michieli Vitturi M, Scarlato P, Andronico D, Scollo S, Kueppers
830 U, Ricci T (2017) Effect of particle volume fraction on the settling velocity of volcanic
831 ash particles: insights from joint experimental and numerical simulations. Scientific
832 Reports 7:39620

833 Di Muro A, Rosi M, Aguilera E, Barbieri R, Massa G, Mundula F, Pieri F (2008) Transport and
834 sedimentation dynamics of transitional explosive eruption columns: The example of the
835 800 BP Quilotoa plinian eruption (Ecuador). Journal of Volcanology and Geothermal
836 Research 174(4):307-324
837 Durant AJ, Rose WI (2009) Sedimentological constraints on hydrometeor-enhanced particle
838 deposition: 1992 Eruptions of Crater Peak, Alaska. Journal of Volcanology and
839 Geothermal Research 186(1-2):40-59
840 Durant AJ, Rose WI, Sarna-Wojcicki AM, Carey S, Volentik ACM (2009) Hydrometeor-
841 enhanced tephra sedimentation: Constraints from the 18 May 1980 eruption of Mount St.
842 Helens. Journal of Geophysical Research 114(B3)
843 Durant AJ, Shaw RA, Rose WI, Mi Y, Ernst GGJ (2008) Ice nucleation and overseeding of ice
844 in volcanic clouds. Journal of Geophysical Research: Atmospheres 113(D9)
845 Durant AJ, Shaw RA, Rose WI, Mi Y, Ernst GGJ (2008) Ice nucleation and overseeding of ice
846 in volcanic clouds. Journal of Geophysical Research: Atmospheres 113(D9):D09206
847 Eckermann SD, Preusse, Peter (1999) Global Measurements of Stratospheric Mountain Waves
848 from Space. Science 286(5444):1534-1537
849 Engwell SL, Eychenne J (2016) Contribution of fine ash to the atmosphere from plumes
850 associated with pyroclastic density currents. In: Mackie S, Ricketts H, Watson M,
851 Cashman K, Rust A (eds) Volcanic Ash: Hazard Observation. Elsevier,
852 Eychenne J, Cashman KV, Rust AC, Durant A (2015) Impact of the lateral blast on the spatial
853 pattern and grain size characteristics of the May 18, 1980 Mount St. Helens fallout
854 deposit. Journal of Geophysical Research 120:6018-6038
855 Eychenne J, Pennec J-L (2012) Sigmoidal particle density distribution in a subplinian scoria
856 fall deposit. Bulletin of Volcanology 74(10):2243-2249

857 Eychenne J, Pennec J-L, Troncoso L, Gouhier M, Nedelec J-M (2012) Causes and
858 consequences of bimodal grain-size distribution of tephra fall deposited during the
859 August 2006 Tungurahua eruption (Ecuador). Bulletin of Volcanology 74(1):187-205
860 Folch A, Costa A, Durant A, Macedonio G (2010) A model for wet aggregation of ash particles
861 in volcanic plumes and clouds: 2. Model application. Journal of Geophysical Research
862 115(B9)
863 Folk RL, Ward WC (1957) Brazos River Bar: a study of the significance of grain size
864 parameters. Journal of Sedimentary Petrology 27:3-26
865 Ganser GH (1993) A rational approach to drag prediction of spherical and nonspherical
866 particles. Powder Technology 77(2):143-152
867 Gardner CA, Cashman KV, Neal CA (1998) Tephra-fall deposits from the 1992 eruption of
868 Crater Peak, Alaska: implications of clast textures for eruptive processes. Bulletin of
869 Volcanology 59:537-555
870 Gilbert JS, Lane SJ (1994) The origin of accretionary lapilli. Bulletin of Volcanology
871 56(5):398-411
872 Hildreth W, Drake RE (1992) Volcan Quizapu, Chilean Andes. Bull Volcanol 54:63-125
873 Horwell C, Baxter P (2006) The respiratory health hazards of volcanic ash: a review for
874 volcanic risk mitigation. Bull Volcanol 69:1 – 24
875 James MR, Gilbert JS, Lane SJ (2002) Experimental investigation of volcanic particle
876 aggregation in the absence of a liquid phase. Journal of Geophysical Research
877 107(B9):2191
878 James MR, Lane SJ, Gilbert JS (2003) Density, construction, and drag coefficient of
879 electrostatic volcanic ash aggregates. Journal of Geophysical Research 108(B9):2435
880 Jenkins SF, Wilson TM, Magill C, Miller V, Stewart C, Blong R, Marzocchi W, Boulton M,
881 Bonadonna C, Costa A (2015) Volcanic ash fall hazard and risk. In: Loughlin SC, Sparks

RSJ, Brown SK, Jenkins SF, Vye-Brown C (eds) Global Volcanic Hazard and Risk. Cambridge Univeristy Press, Cambridge

Jiang Q, Doyle JD (2004) Gravity Wave Breaking over the Central Alps: Role of Complex Terrain. Journal of the Atmospheric Sciences 61(18):2249-2266

Jones TJ, McNamara K, Eychenne J, Rust AC, Cashman KV, Scheu B, Edwards R (2016) Primary and secondary fragmentation of crystal-bearing intermediate magma. Journal of Volcanology and Geothermal Research 327:70-83

Jones TJ, Russell JK (2017) Ash production by attrition in volcanic conduits and plumes. Scientific Reports 7(1):5538

Kueppers U, Cimarelli C, Hess K-U, Taddeucci J, Wadsworth F, Dingwell D (2014) The thermal stability of Eyjafjallajokull ash versus turbine ingestion test sands. Journal of Applied Volcanology 3(1):4

Larsson W (1937) Vulkanische Asche vom Ausbruch des chilenischen Vulkans Quizapu (1932) in Argentina gesammelt. Geol Inst Upsala Bull 26:27-52

Lovell CJ, Rose CW (1991) Wake-Capture Effects Observed in a Comparison of Methods to Measure Particle Settling Velocity Beyond Stokes' Range. Journal of Sedimentary Research 61:575-582

Manzella I, Bonadonna C, Phillips JC, Monnard H (2015) The role of gravitational instabilities in deposition of volcanic ash. Geology 43:211-214

Mastin LG, Van Eaton AR, Durant AJ (2016) Adjusting particle-size distributions to account for aggregation in tephra-deposit model forecasts. Atmos. Chem. Phys. 16(14):9399-9420

Maxey MR (1987) The gravitational settling of aerosol particles in homogeneous turbulence and random flow fields. Journal of Fluid Mechanics 174:441-465

Maxey MR, Corrsin S (1986) Gravitational Settling of Aerosol Particles in Randomly Oriented Cellular Flow Fields. Journal of the Atmospheric Sciences 43(11):1112-1134

McGimsey RG, Neal CA, Riley CM (2001) Areal distribution, thickness, mass, volume and grainsize of tephra-fall deposits from the 1992 eruptions of Creater Peak vent, Mt. Spurr Volcano, Alaska. U.S. Geological Survey Open-File Report 01-370

Miller TP, Neal CA, Waitt RB (1995) Pyroclastic Flows of the 1992 Crater Peak Eruptions: Distribution and Origin. In: Keith TEC (ed) The 1992 eruptions of Crater Peak vent, Mount Spurr volcano, Alaska. USGS Bulletin 2139. USGS, Washington, pp 81-88

Neal CA, McGimsey RG, Gardner CA, Harbin ML, Nye CJ (1995) Tephra-fall Deposits from the 1992 Eruptions of Crater Peak, Mount Spurr Volcano, Alaska: A Preliminary Report on Distribution, Stratigraphy, and Composition. In: Keith TEC (ed) The 1992 eruptions of Crater Peak vent, Mount Spurr volcano, Alaska. USGS Bulletin 2139. USGS, Washington, pp 65-80

Poulidis AP, Takemi T, Iguchi M, Renfrew IA Orographic effects on the transport and deposition of volcanic ash: A case study of Mt. Sakurajima, Japan. Journal of Geophysical Research: Atmospheres. DOI: 10.1002/2017JD026595

Pyle DM (1989) The thickness, volume and grainsize of tephra fall deposits. Bulletin of Volcanology 51:1-15

Riley CM, Rose WI, Bluth GJS (2003) Quantitative shape measurements of distal volcanic ash. Journal of Geophysical Research: Solid Earth 108(B10):2504

Roman DC, Moran SC, Power JA, Cashman KV (2004) Temporal and Spatial Variation of Local Stress Fields before and after the 1992 Eruptions of Crater Peak Vent, Mount Spurr Volcano, Alaska. Bulletin of the Seismological Society of America 94(6):2366-2379

Rose W, Bluth GJS, Schneider D, Ernst G, Riley CM, Henderson LJ, McGimsey RG (2001) Observations of Volcanic Clouds in Their First Few Days of Atmospheric Residence: The 1992 Eruptions of Crater Peak, Mount Spurr Volcano, Alaska. The Journal of Geology 109(6):677-694

Rose W, Durant A (2009) Fine ash content of explosive eruptions. J Volcanol Geotherm Res 186:32 - 39

Rose WI, Durant AJ (2011) Fate of volcanic ash: Aggregation and fallout. Geology 39(9):895-896

Rose WI, Kostinski A, Kelley L (1995) Real-time C-band Radar Observations of 1992 Eruption Clouds from Crater Peak, Mount Spurr Volcano, Alaska. In: Keith TEC (ed) The 1992 eruptions of Crater Peak vent, Mount Spurr volcano, Alaska. USGS Bulletin 2139. USGS, Washington, pp 19-26

Sarna-Wojcicki A, Shipley S, Waitt RB, Dzurisin D, Wood S (1981) Aeral distribution, thickness , mass, volume and grain size of air-fall ash from the six major eruptions of 1980. U.S. Geological Survey Professional Paper 1250:577-600

Scasso RA, Corbella H, Tiberi P (1994) Sedimentological analysis of the tephra from the 12–15 August 1991 eruption of Hudson volcano. Bulletin of Volcanology 56(2):121-132

Schneider D, Rose WI, Kelley L (1995) Tracking of 1992 Eruption Clouds from Crater Peak Vent of Mount Spurr Volcano, Alaska, Using AVHRR. In: Keith TEC (ed) The 1992 eruptions of Crtaer Peak vent, Mount Spurr volcano, Alaska. USGS Bulletin 2139. USGS, Washington, pp 27-36

Schumacher R, Schmincke H-U (1995) Models for the origin of accretionary lapilli. Bulletin of Volcanology 56(8):626-639

Sorem RK (1982) Volcanic ash clusters: Tephra rafts and scavengers. Journal of Volcanology and Geothermal Research 13(1–2):63-71

Sparks RSJ, Bursik MI, Ablay GJ, Thomas RME, Carey SN (1992) Sedimentation of tephra by volcanic plumes. Part 2: controls on thickness and grain-size variations of tephra fall deposits. Bulletin of Volcanology 54(8):685-695

956 Taddeucci J, Scarlato P, Montanaro C, Cimarelli C, Del Bello E, Freda C, Andronico D,
957 Gudmundsson MT, Dingwell DB (2011) Aggregation-dominated ash settling from the
958 Eyjafjallajokull volcanic cloud illuminated by field and laboratory high-speed imaging.
959 Geology 39(9):891-894
960 Thielen J, Wobrock W, Gadian A, Mestayer P, Creutin J-D (2000) The possible influence of
961 urban surfaces on rainfall development: a sensitivity study in 2D in the meso-γ-scale.
962 Atmospheric Research 54(1):15-39
963 Van Eaton A, Muirhead J, Wilson CN, Cimarelli C (2012) Growth of volcanic ash aggregates
964 in the presence of liquid water and ice: an experimental approach. Bulletin of
965 Volcanology 74(9):1963-1984
966 Walker GPL (1981) Generation and dispersal of fine ash and dust by volcanic eruptions. Journal
967 of Volcanology and Geothermal Research 11(1):81-92
968 Watanabe K, Ono K, Sakaguchi K, Takada A, Hoshizumi H (1999) Co-ignimbrite ash-fall
969 deposits of the 1991 eruptions of Fugen-dake, Unzen Volcano, Japan. Journal of
970 Volcanology and Geothermal Research 89(1–4):95-112
971 Watt SFL, Gilbert JS, Folch A, Phillips JC, Cai XM (2015) An example of enhanced tephra
972 deposition driven by topographically induced atmospheric turbulence. Bulletin of
973 Volcanology 77(5):1-14
974 Watt SFL, Pyle DM, Mather TA, Martin RS, Matthews NE (2009) Fallout and distribution of
975 volcanic ash over Argentina following the May 2008 explosive eruption of Chaitén,
976 Chile. J. Geophys. Res. 114(B4):B04207
977 Webley PW (2015) Volcanoes and the aviation industry. In: Loughlin SC, Sparks RSJ, Brown
978 SK, Jenkins SF, Vye-Brown C (eds) Global Volcanis Hazards and risk. Cambridge
979 University Press, Cambridge

White JT, Connor CB, Connor L, Hasenaka T (2017) Efficient inversion and uncertainty quantification of a tephra fallout model. Journal of Geophysical Research: Solid Earth 122(1):281-294

Wiesner MG, Wetzel A, Catane SG, Listanco EL, Mirabueno HT (2004) Grain size, areal thickness distribution and controls on sedimentation of the 1991 Mount Pinatubo tephra layer in the South China Sea. Bulletin of Volcanology 66(3):226-242

Wilson TM, Jenkins SF, Stewart C (2015) Volcanic ash fall impact. In: Loughlin SC, Sparks RSJ, Brown SK, Jenkins SF, Vye-Brown C (eds) Global Volcanic Hazards and Risk. Cambridge University Press, Cambridge

Wobrock W, Flossmann AI, Monier M, Pichon J-M, Cortez L, Fournol J-F, Schwarzenböck A, Mertes S, Heintzenberg J, Laj P (2001) The Cloud Ice Mountain Experiment (CIME) 1998: experiment overview and modelling of the microphysical processes during the seeding by isentropic gas expansion. Atmospheric research 58(4):231-265

Wright HMN, Cashman K, Mothes PA, Hall ML, Ruiz GA, Le Pennec JL (2012) Estimating rates of decompression from textures of erupted ash particles produced by 1999–2006 eruptions of Tungurahua volcano, Ecuador. Geology 40(7):619-622